Supporting Information for:

Broadband absorption engineering to enhance light absorption in monolayer MoS_2

Shah Mohammad Bahauddin[†,∥,⊥], *Hossein Robatjazi*[†,∥,⊥] *and Isabell Thomann*[*†,‡,§,∥,⊥]

[†]Department of Electrical and Computer Engineering, ‡Department of Materials Science and NanoEngineering, §Department of Chemistry, ∥Laboratory for Nanophotonics, and ⊥Rice Quantum Institute, Rice University, 6100 Main Street, Houston, Texas 77005, United States.

* Email: isabell.thomann@rice.edu

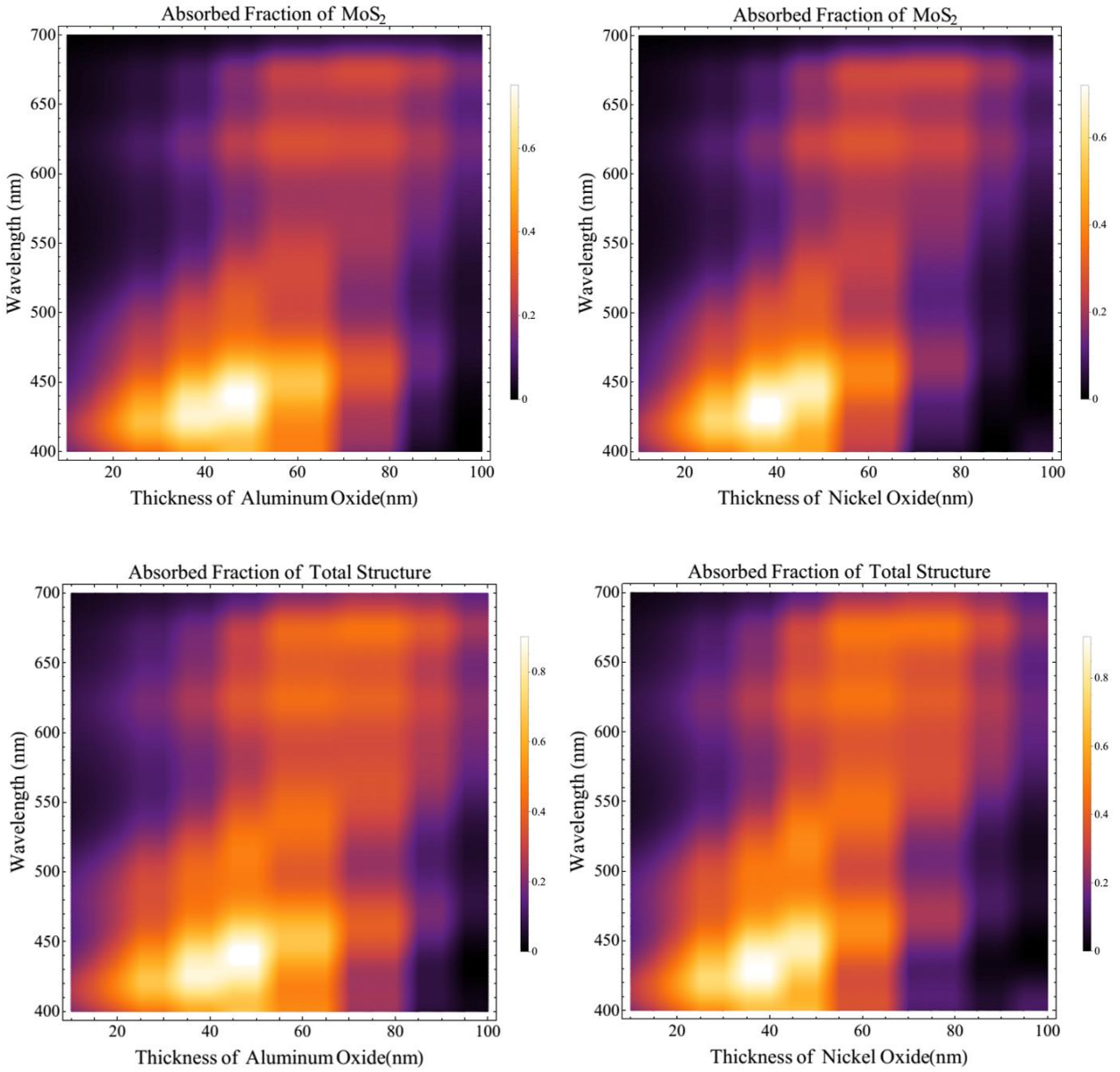

Figure S1: Fraction of incident light absorbed within monolayer MoS_2 (top) and in the total structure (bottom), as a function of wavelength and thickness of the spacer layer, as determined by FDTD simulations. The panels at the left side correspond to structures with an Al_2O_3 spacer layer and the panels at the right side correspond to ones with a NiO_x spacer layer. The contour plots show that maximum absorption can be obtained for 45 nm Al_2O_3 and 40 nm NiO_x thick spacer layers, respectively.

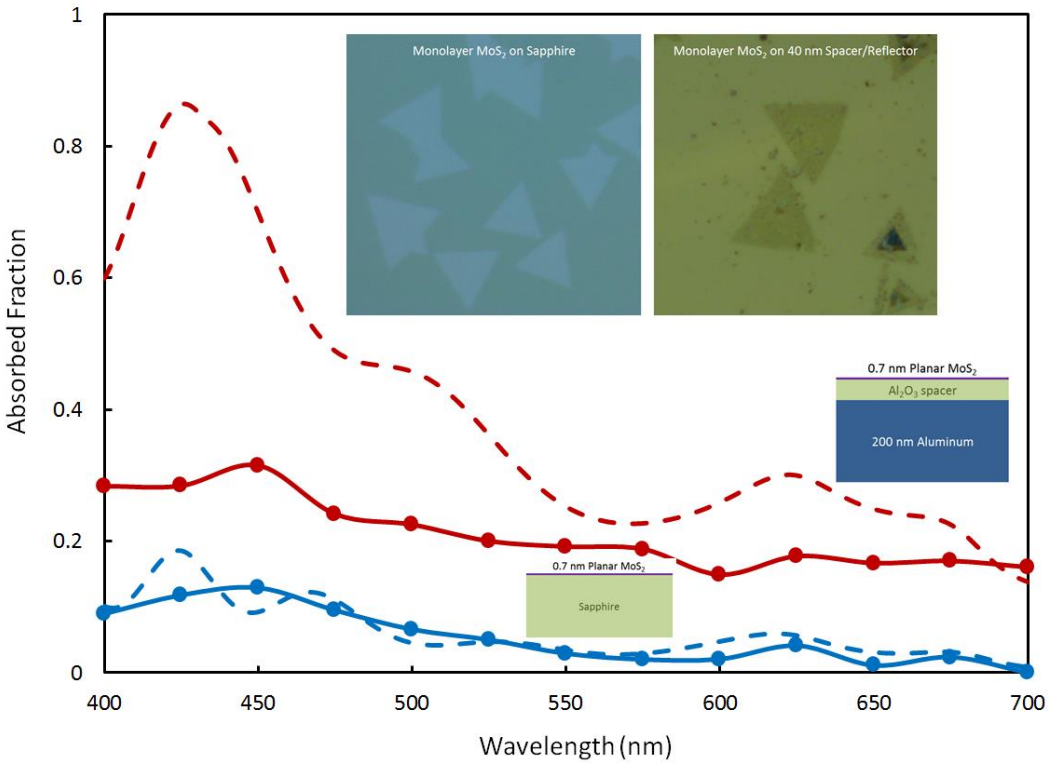

Figure S2: Experimentally measured absorbed fraction of incident light vs. wavelength for MoS_2 on a sapphire (Al_2O_3) substrate and MoS_2/40 nm Al_2O_3/Al structures we used for PL measurements. Reflection microscopy images (panels at the top) of monolayer MoS_2/ 40 nm Al_2O_3/Al (right) also reveal the enhanced absorption compared to that of monolayer MoS_2/Al_2O_3 (sapphire) (left). The color contrast of the monolayer MoS_2 on top of the sapphire substrate shows that the MoS_2 flakes are reflecting while most of the light is transmitted through the bare sapphire substrate. However, the contrast is reversed when we placed monolayer MoS_2 on the 40 nm Al_2O_3 spacer/Al substrate. In this case, the light is reflected by the Al_2O_3 spacer/ reflector but the MoS_2 appears darker in color hinting at the higher absorption within the monolayer. The experimentally measured fraction of light absorbed in these structures, when integrated from 400 to 700 nm, is 21.1% for MoS_2/40 nm Al_2O_3/Al, compared to 5.5% for MoS_2/Al_2O_3, i.e. there is an absorption enhancement of 3.9 x *in the total structure*. Note that our simulations predict an integrated absorbed fraction of up to 33 % for an optimally impedance matched architecture that

would require a slightly thicker spacer layer of 45 nm Al_2O_3. Note that the absorption spectra calculated by FDTD exhibit slight oscillatory artifacts arising from a polynomial fit to the real and imaginary part of the dielectric constant that causes an overestimation of the absorption around 440 nm.

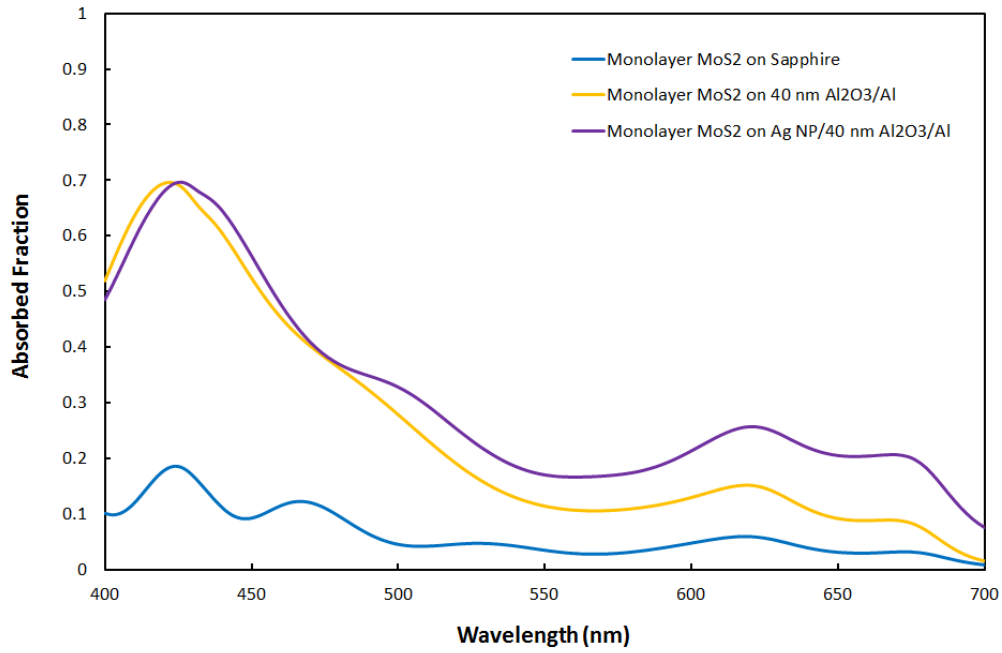

Figure S3: Simulated fraction of light absorbed within a monolayer of MoS_2, as a function of wavelength (i) on Al_2O_3 (blue line), (ii) on 40 nm Al_2O_3/ Al (red line), and (ii) on Ag nanoparticles/Al_2O_3/ Al (green line). These simulation results predict absorption enhancements within the 7Å thick monolayer MoS_2 when placed on substrates (ii) and (iii).

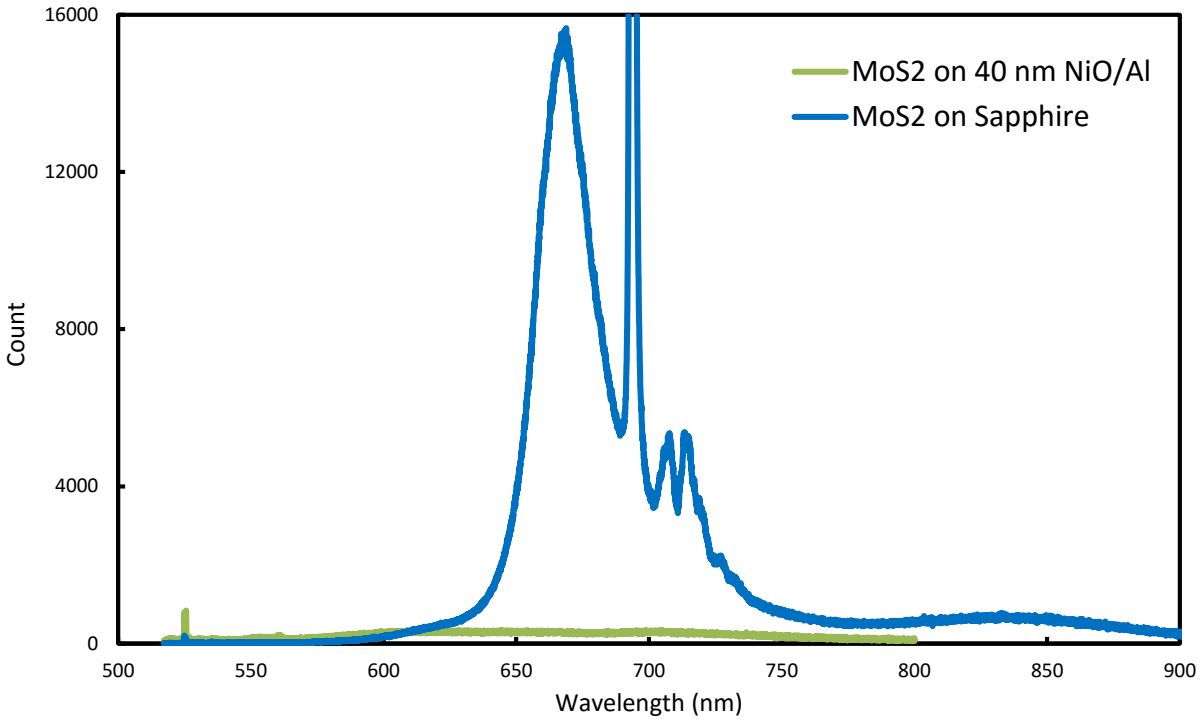

Figure S4: Photoluminescence quenching spectra, excited at 514.5 nm, for (i) MoS_2 on Al_2O_3 (blue) and (ii) our target structure MoS_2 on NiO_x/Al designed for efficient charge carrier separation (green). While absorption characteristics between Al_2O_3/Al and NiO_x/Al structures are similar, MoS_2 on NiO_x/Al shows severe quenching of the photoluminescence signal which we attribute to hole scavenging by the underlying NiO_x substrate (green).

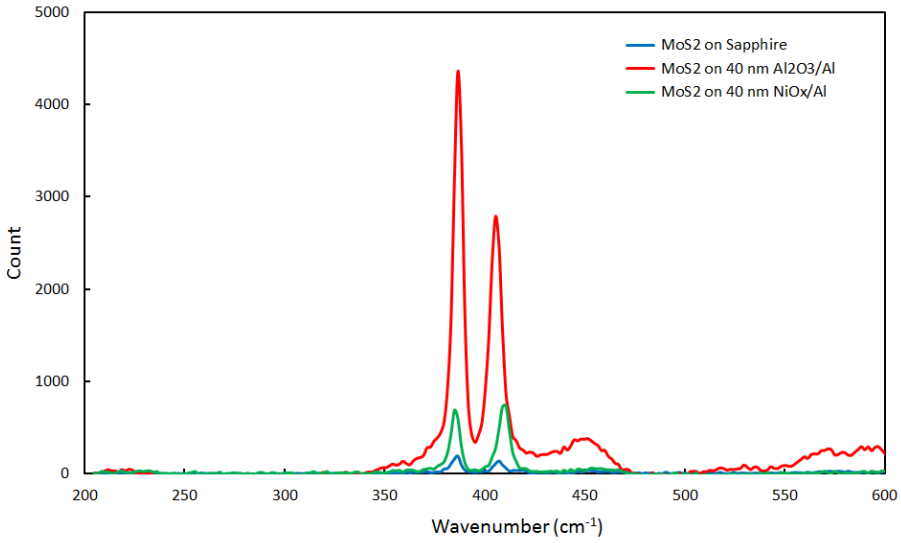

Figure S5: Measured Raman signals for monolayer MoS_2 on sapphire (blue solid line), on 40 nm Al_2O_3/Al (red solid line), and on 40 nm NiO_x/Al (green solid line). The excitation wavelength was 514.5 nm and the laser power was 1.25 mW.

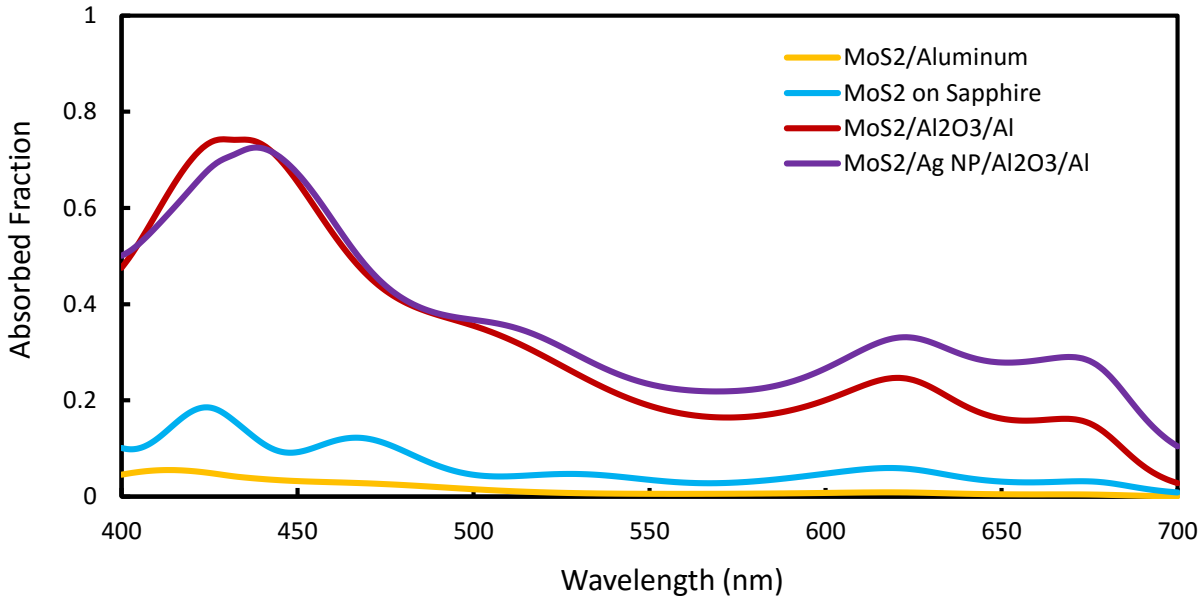

Figure S6: FDTD simulation of absorbed fraction of incident light within MoS_2 vs. wavelength for different substrates: MoS_2 on Aluminum, Sapphire, Al_2O_3/Al and AgNPs/Al_2O_3/Al. It should be noted that placing MoS_2 directly on an Al reflector instead of using an optical cavity such as MoS_2/Al_2O_3/Al or MoS_2/NiO_x/Al does lead to an inferior absorbed fraction within MoS_2.

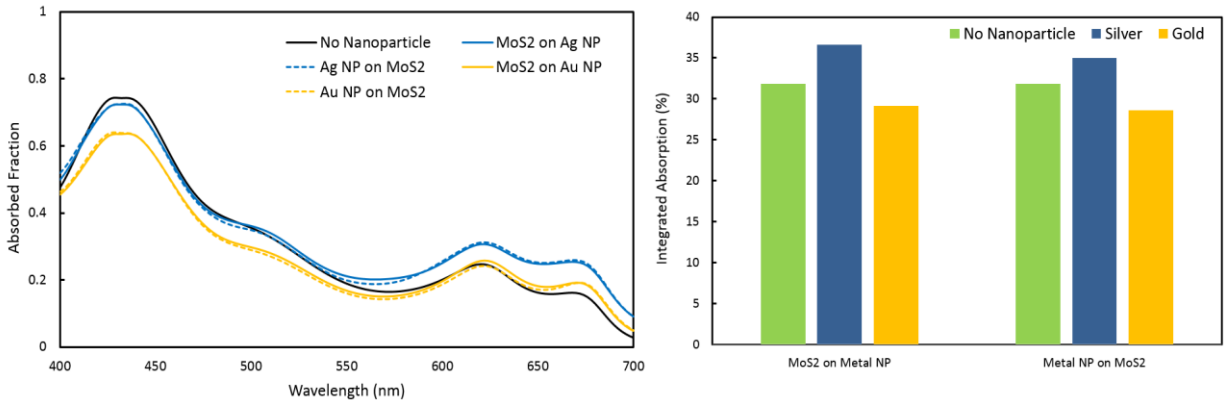

Figure S7: FDTD simulations of the wavelength dependence of the absorbed fraction and corresponding integrated absorbed fraction from 400 to 700 nm for various configurations. The thickness of the Al_2O_3 spacer layer is 45 nm, the thickness and diameter of the Ag nanodisks are 5 nm and 30 nm, respectively. We kept the fill fraction of silver w.r.t. to air fixed at 0.36. As a point of reference, the plasmon resonance of gold disks on the Al_2O_3/Al structure is around 800 nm, and for silver disks around 650 nm without MoS_2. The maximum absorption enhancement can be achieved when the Ag nanodisks are placed below MoS_2. For Au nanodisks, a small absorption enhancement can be achieved at wavelengths longer than 630 nm, however the integrated absorption is suppressed compared to that without plasmonic nanoparticles.

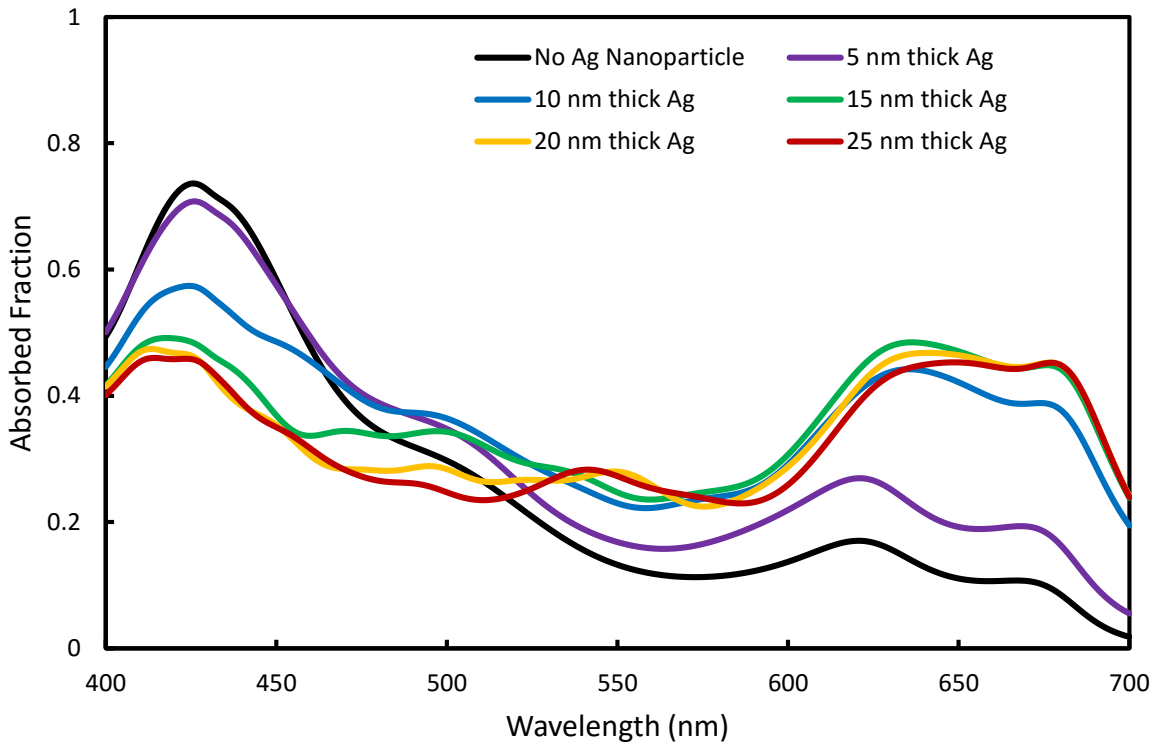

Figure S8: FDTD simulations of the absorbed fraction within the MoS_2 monolayer vs. wavelength for different thicknesses of Ag nanodisks (30 nm diameter) on a 45 nm thick Al_2O_3 spacer /aluminum reflector substrate.

S9: FDTD Simulation Details

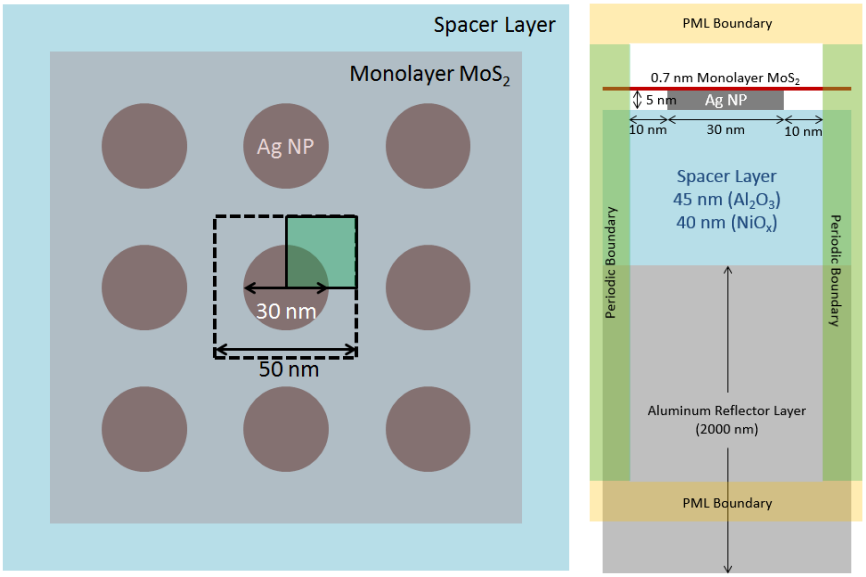

Figure S9: Left: Simulation setup of the materials in the XY plane in FDTD simulations (Lumerical commercial software package): the green area represents the simulation region. E-field points in X-direction. Along the boundaries parallel to the E-field, perfect magnetic conductor boundary conditions were applied. Along the boundaries perpendicular to the E-field, perfect electric conductor boundary conditions were applied. Right: Simulation setup in the XZ plane. The coordinate of the MoS_2 layer is from (x, y, z = 0) to (x, y, z = 0.7 nm). The Ag and MoS_2 area is meshed by mesh cells of 0.05 nm. All other parts of the simulation are meshed by cells of 1 nm. The PML area extends from z = -1000 nm to z = +1000 nm. Plane waves are launched from z = 900 nm towards the device.

Commercial grade software (Lumerical FDTD Solutions), a 3D Maxwell solver, was used to analyze the response of our nanostructure. Using Lumerical, a square array of Ag nanodisks was simulated on top of a Al_2O_3 (or NiO_x) spacer layer/Al reflector. Monolayer MoS_2 was set on top of the structure that has a thickness of 0.7 nm and we investigated the absorption properties of the MoS_2 within a 400 nm to 700 nm wavelength range. The refractive indices of the MoS_2, Al_2O_3 and

NiO_x were inserted into Lumerical from our measured uv-visible absorption data. In the simulation, the polarization of the E-field was set along the X-axis and the polarization of the H-field was set along the Y-axis. Propagation of light was set along the Z-axis. To simulate an array of nanodisks, symmetric boundary conditions were applied along the X and Y axes. Symmetric boundary conditions are used since our structure exhibits multiple planes of symmetry. "Symmetric boundaries are mirrors for the electric field, and anti-mirrors for the magnetic field" [Reference:http://docs.lumerical.com/en/ref_sim_obj_symmetric_anti-symmetric.html, http://docs.lumerical.com/en/ref_sim_obj_boundary_conditions_tab.html]. By taking advantage of the periodic structure and symmetry of our setup, we utilized this boundary condition to reduce the simulation volume and time by a factor of 4. Next Perfectly Matched Layer (PML) boundary was applied at the Z axes. PML boundaries absorb electromagnetic waves incident upon them and thus simulate near reflection-less (10^{-5} in our case) boundaries. The PML boundary at the negative Z-axis was extended through the structure (in this case aluminum) from z = -1000 nm for better absorption of light. A plane wave is launched from 100 nm below the upper positive PML where this upper PML is placed at 1000 nm above the (x, y, 0) surface. Hence, the total length of the simulation region along the Z-axis is 2000 nm. The background refractive index of the simulation was set as 1 which is the refractive index of air. Finally, the simulation was run for 2000 femtoseconds (fs) to ensure steady state results. In FDTD, the electric field is monitored and stored in a data file which is used to calculate the power absorbed as a function of wavelength using the equation, $P_{Abs}(\lambda) = \frac{\epsilon_0}{2} \int Imag[\epsilon(\lambda)]\omega(\lambda)|E(x,y,z,\lambda)|^2 dV$, where $\omega(\lambda) = c\ 2\pi/\lambda$.

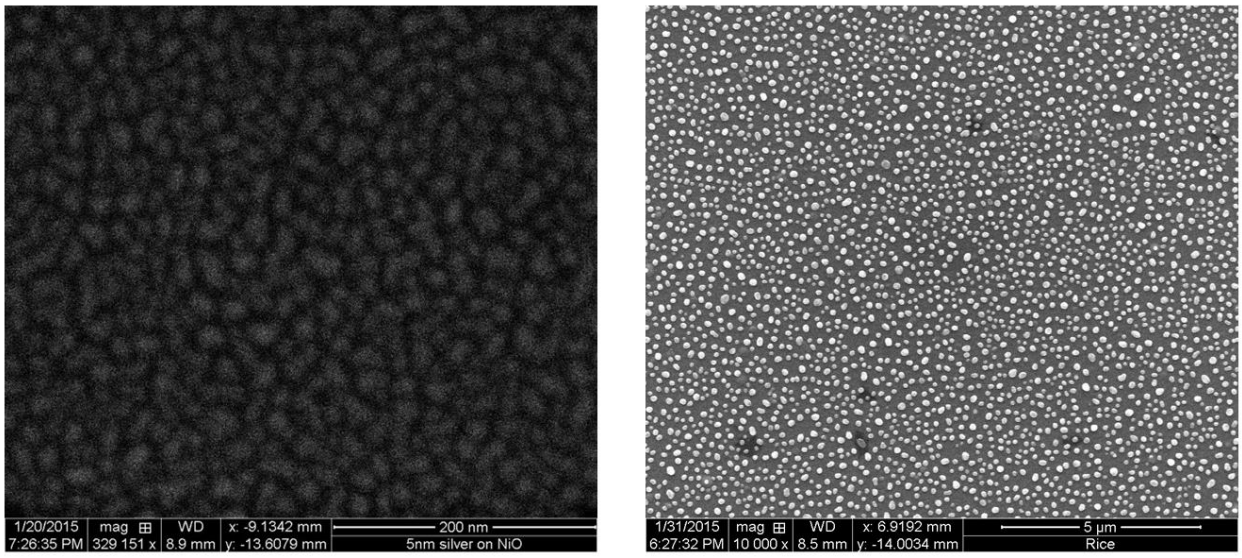

Figure S10: Scanning electron microscope images of 5 nm and 7 nm thick Ag nanoparticles on top of a NiO_x spacer layer.

S11: Effective medium model for plasmonic metamaterial MoS_2/Ag/air

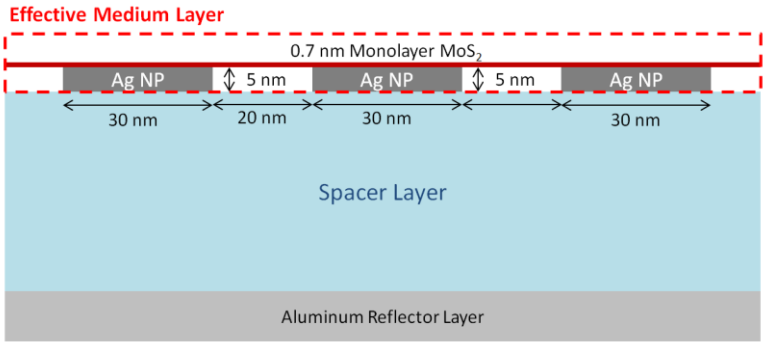

Figure S11 A: Schematic of effective medium of the nanostructure. The thickness of the spacer layer is 45 nm for Al_2O_3 and 40 nm for NiO_x. The 2D Bruggeman model was applied to the Ag/air semiconducting-like layer and is combined with MoS_2 employing the generalized effective medium approach.

We devised a plasmonic metamaterial consisting of three components, monolayer MoS_2 and Ag nanodisks (30 nm diameter by 5 nm thick) embedded in air, that closely resembles our experimentally realized structure (Figure S11 A). First we employed the effective medium theory by Bruggeman in two dimensions [1] to find the effective dielectric constant for a two-component system of Ag nanoparticles and air. In our case this material behaves semiconductor-like (see Figure S11 B). We found that the Bruggeman model yields better agreement with the electromagnetic simulations than the Maxwell-Garnett mixing rule (Figure 6). Then we used the generalized effective medium approach to combine this Ag/air composite with the thin MoS_2 monolayer. We then calculated the real and imaginary refractive index for an effective medium layer that fulfills the critical coupling condition [2,3] to predict the fill fraction of Ag nanodisks in air that minimizes the mismatch of our 3-component plasmonic metamaterial to the effective medium of the critical coupling condition. Using this optimum 3-component effective medium,

we then used the transfer matrix formalism to determine analytically the optimum spacer layer thickness using the complex refractive index for the aluminum back reflector.

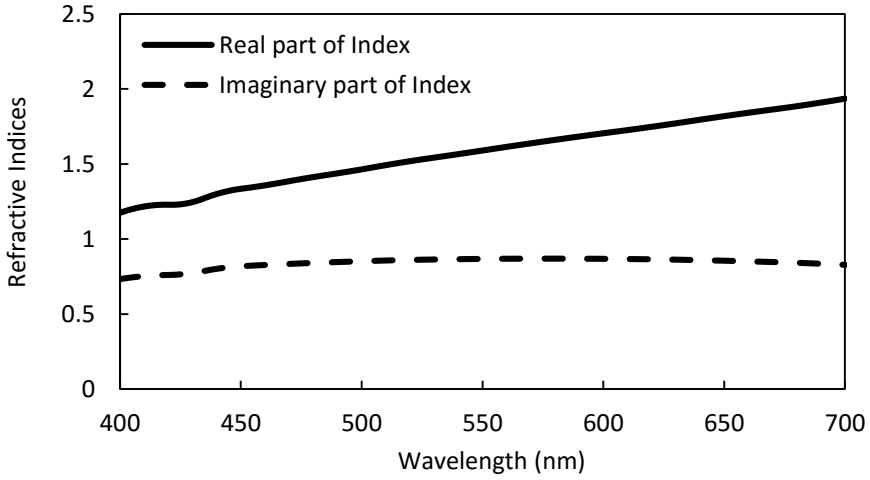

Figure S11 B: Real and imaginary part of the Ag/air layer calculated by the 2D Bruggeman model. Here, $\eta > \kappa$, meaning this combined material behaves semiconductor-like.

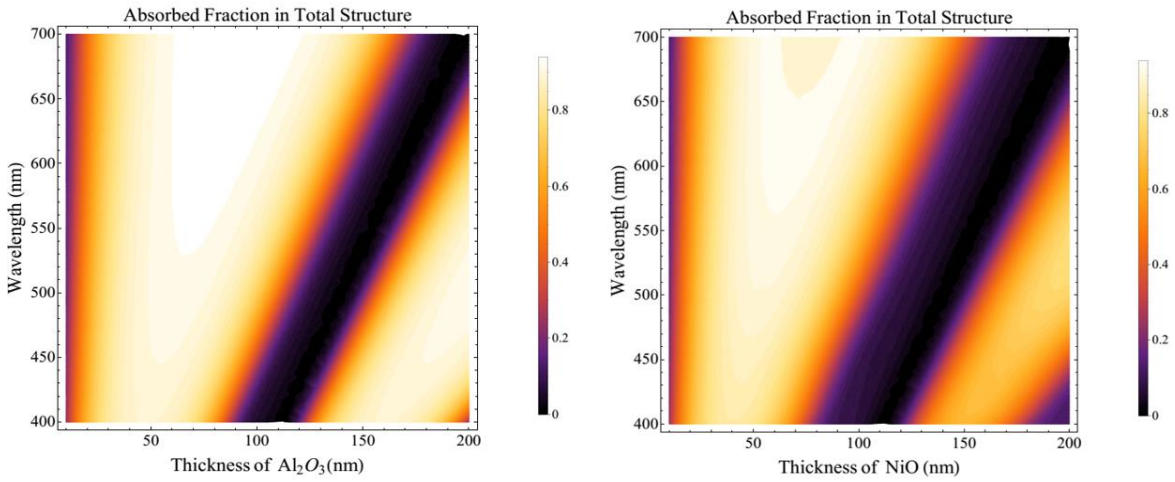

Figure S12: Theoretical maximum absorption in total structure is calculated by the critical coupling model and the dependences of absorption as a function of Al_2O_3 spacer thicknesses (Left) and NiO_x (Right). The model assumes a perfect electric conductor reflector, and therefore the spacer layer thickness is overestimated by the skin depth of aluminum which varies from 11.6 nm to 13.15 nm in the 400 to 700 nm wavelength region.

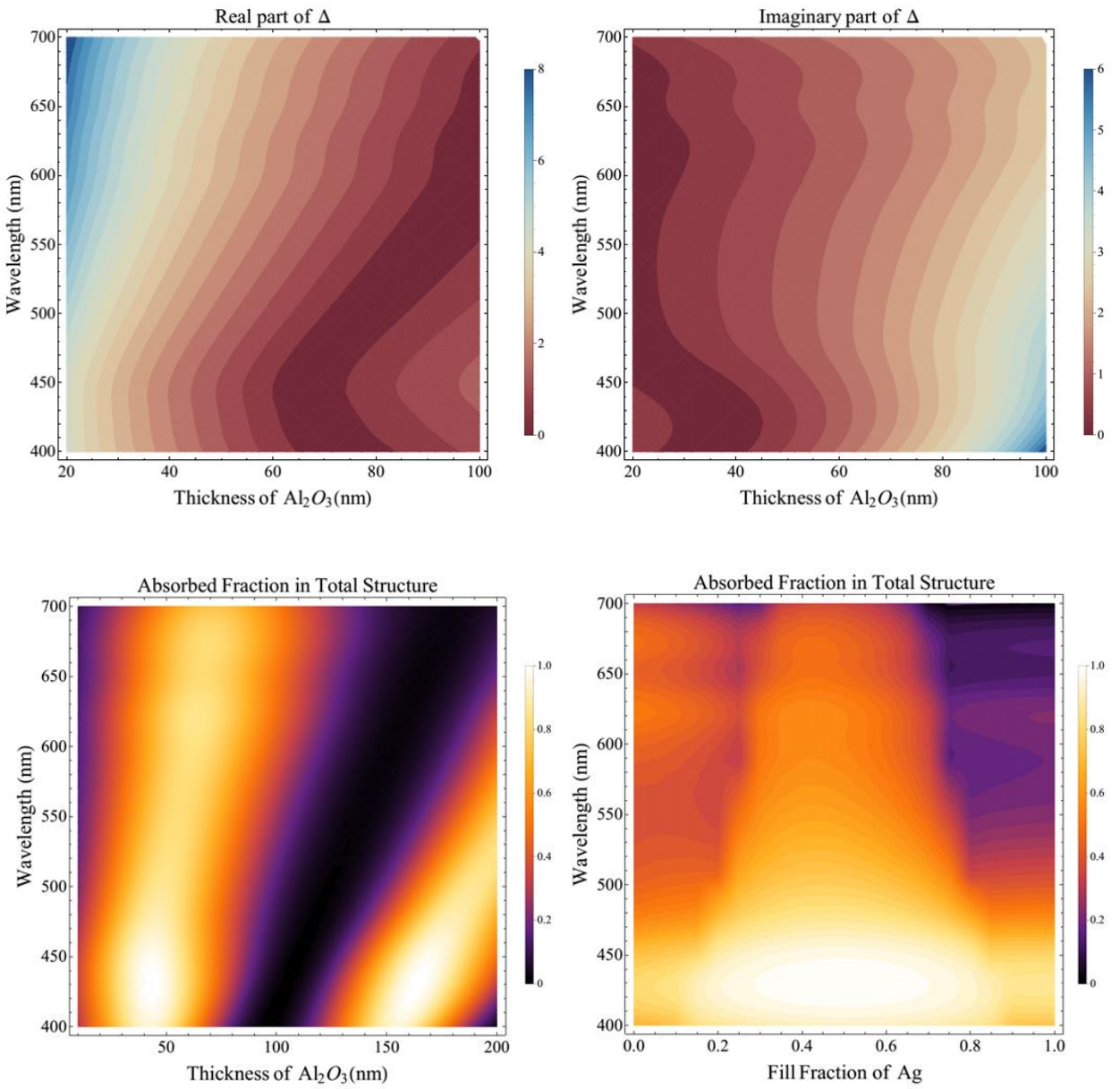

Figure S13: Top left: Wavelength dependence of the mismatch of the real part of the refractive index of our effective medium layer consisting of monolayer MoS_2/ 30 nm diameter, 5 nm thick Ag nanodisks/ air w.r.t. the critical coupling condition [2] for different thicknesses of the Al_2O_3 spacer layer. Theoretically zero mismatch is required at all wavelengths to achieve broadband near unity absorption. Top right: Wavelength dependence of the mismatch of the imaginary part of the refractive index. Bottom left: Absorbed fraction of the incident light in the total structure as a

function of wavelength and Al_2O_3 spacer thickness determined by the transfer matrix model with an effective medium layer employing a fixed fill fraction of Ag w.r.t air of 0.36. The fill fraction of MoS_2 is 0.123. Bottom right: Absorbed fraction of the incident light in the total structure as a function of wavelength and Ag nanoparticle fill fraction determined by the transfer matrix model with a Bruggeman model effective medium layer, and at a fixed 45 nm Al_2O_3 spacer thickness.

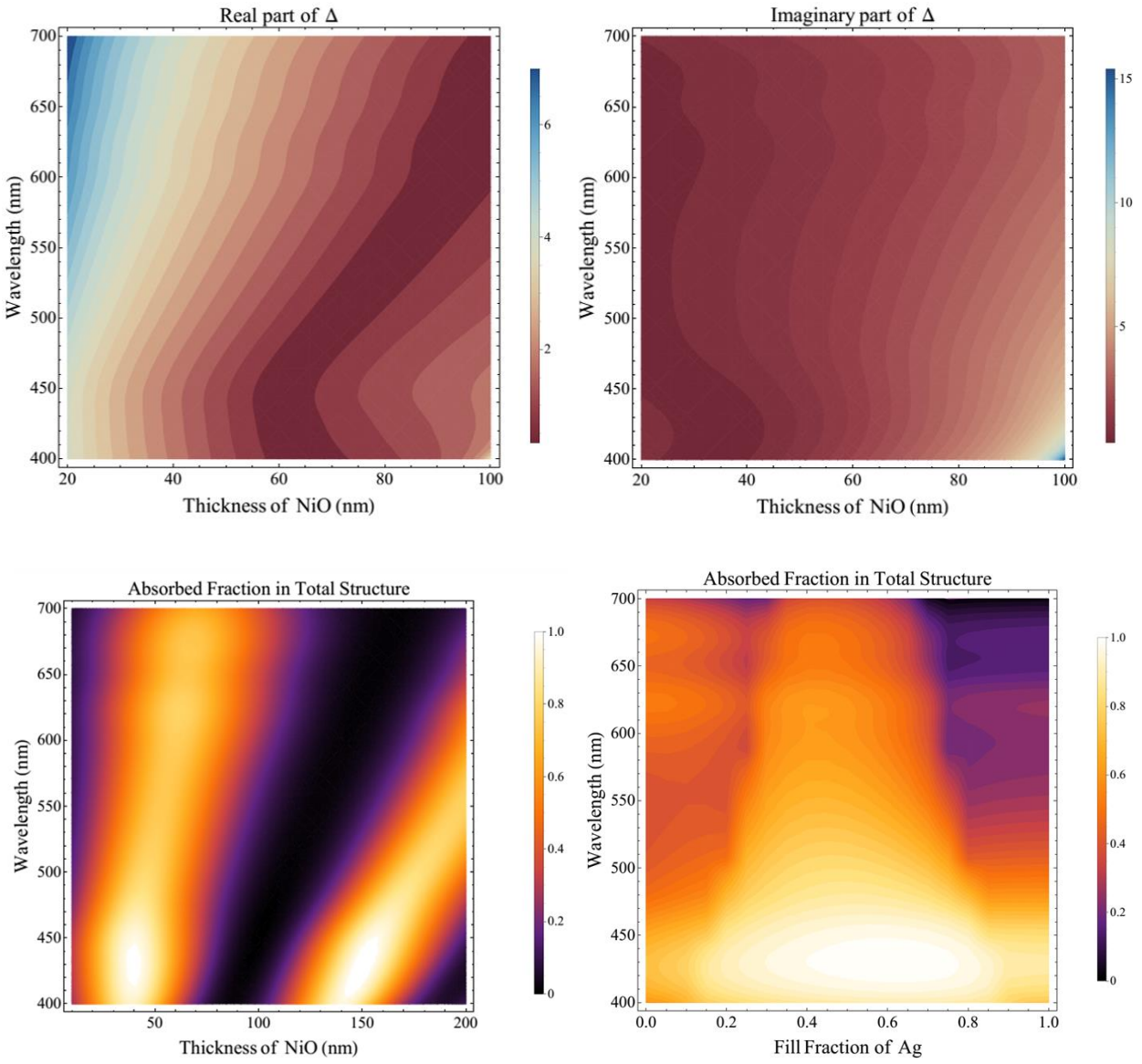

Figure S14: Top left: Wavelength dependence of the mismatch of the real part of the refractive index of our effective medium layer consisting of monolayer MoS_2/ 30 nm diameter, 5 nm thick Ag nanodisks/ air w.r.t. the critical coupling condition [2,3] for different thicknesses of the NiO_x spacer layer. Theoretically zero mismatch is required at all wavelengths to achieve broadband near unity absorption. Top right: Wavelength dependence of the mismatch of the imaginary part of the refractive index. Bottom left: Absorbed fraction of the incident light in the total structure as a function of wavelength and NiO_x spacer thickness determined by the transfer matrix model with

an effective medium layer employing a fixed fill fraction of Ag w.r.t air of 0.36. The fill fraction of MoS_2 is 0.123. Bottom right: Absorbed fraction of the incident light in the total structure as a function of wavelength and Ag nanoparticle fill fraction determined by the transfer matrix model with a Bruggeman model effective medium layer, and at a fixed 40 nm NiO_x spacer thickness.

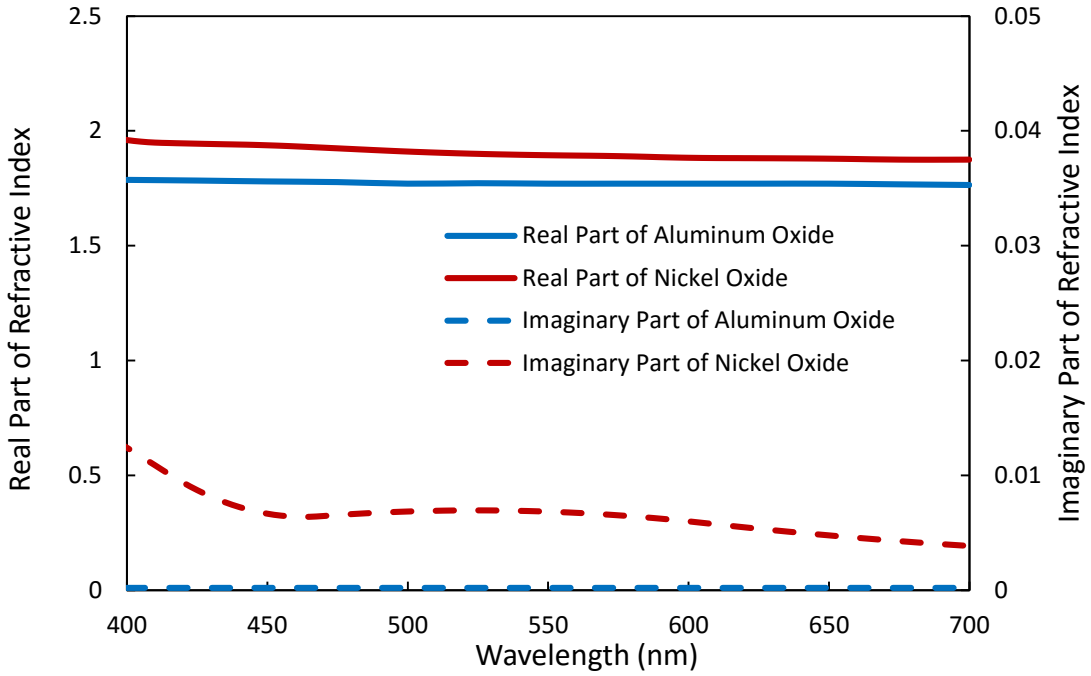

Figure S15: Real and imaginary part of the refractive indices of the spacer layers we used for this experiment: aluminum oxide and nickel oxide. The refractive index for aluminum oxide was acquired by spectroscopic ellipsometry, whereas the one for nickel oxide was calculated from reflection and transmission measurements as a function of wavelength with an integrating sphere.

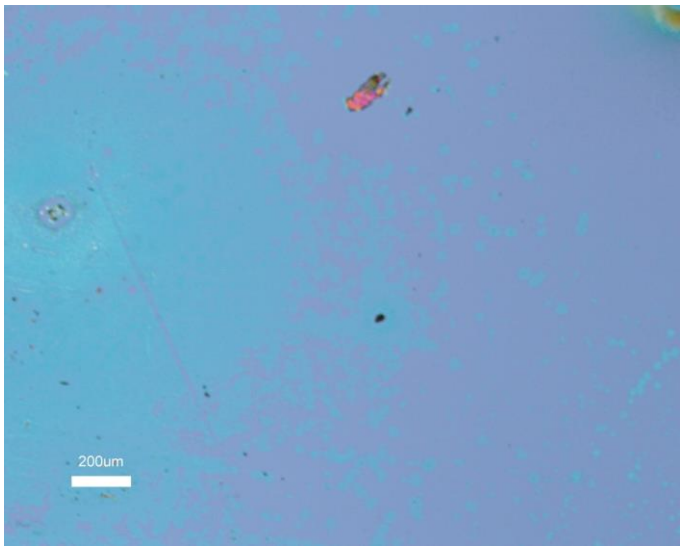

Figure S16: Microscope image of millimeter scale as-grown single layer MoS_2 (bright blue) on top of SiO_2/Si substrate. Details of the growth process are described in the main text.

S17: Design criteria for the spacer layer

We note that the dielectric spacer layer in our structures should be optically transparent so that no light is absorbed by the spacer itself. Moreover, since we intend to utilize this structure as a photocathode in which MoS_2 simultaneously serves as a light absorber and catalyst for the hydrogen evolution reaction, we also require the dielectric spacer layer to allow for efficient charge separation at the MoS_2/ dielectric spacer interface and transport of holes to the aluminum back electrode/reflector, in addition to forming a photonic cavity. Among wide band gap metal oxides, titanium dioxide (TiO_2), zinc oxide (ZnO), indium tin oxide (ITO), fluorine-doped tin oxide (FTO) and nickel oxide (NiO_x) are widely employed transparent conductive electrodes[4-7]. Here, we chose NiO_x as the dielectric spacer layer[8] since it is a p-type semiconductor with a large bandgap of 3.5 eV and high optical transparency, and the band edges are favorable for selective hole scavenging from the photoactive monolayer of MoS_2. To predict the dimension resulting in optimum

absorption within the monolayer MoS_2, we optimized the spacer thickness using finite difference time domain (FDTD) simulations. The optimized spacer thickness can alternatively be predicted within 5 nm using a transfer matrix formalism.

S18: Effect of MoS_2 incorporation and multiple diameter NP distribution on the Absorption of Ag

Since it is not experimentally feasible to directly measure the absorption of Ag nanoparticles after the MoS_2 has been transferred on top of the structures, we have simulated the absorption within Ag NPs with and without a MoS_2 top layer. The results (shown in the Figure below) show that absorption within the Ag nanoparticles is strongly reduced in the presence of a top monolayer of MoS_2. This phenomenon presents a unique opportunity to design photoelectrode structures that minimize the lossy effects of metal nanoparticles on photoelectrode performance.

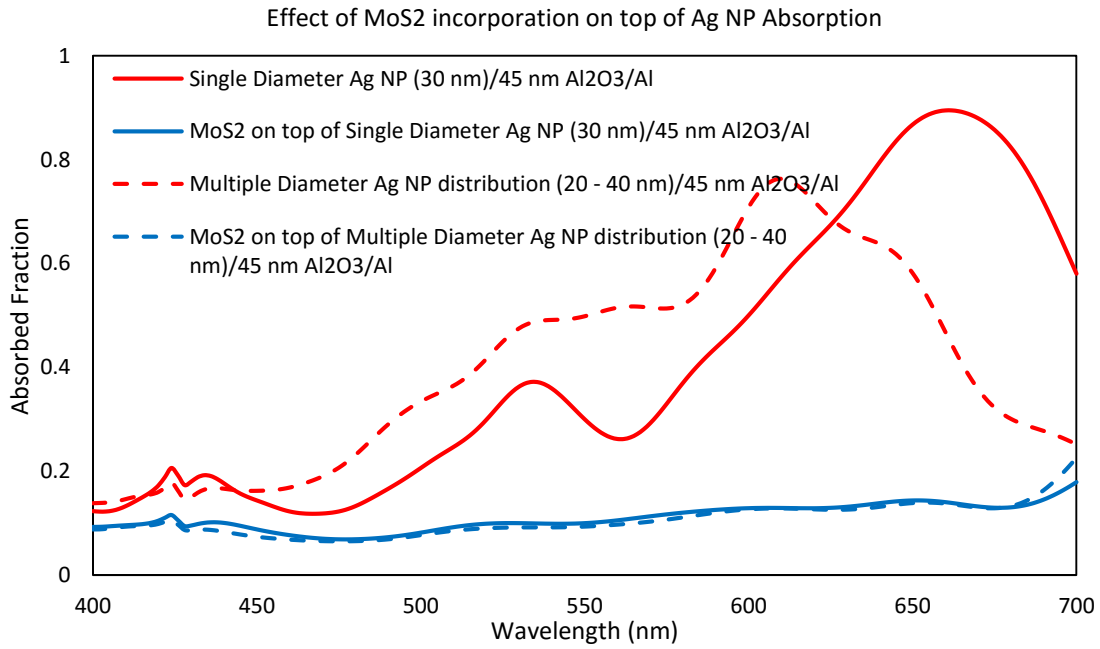

The strongly reduced absorption in Ag holds equally in the case of a polydisperse Ag particle diameter distribution. Practically, e-beam evaporation of a polydisperse Ag nanoparticle size distribution is a simple means to increase absorption within MoS_2. In conclusion, adding a MoS_2 top layer to the cavity structure reduces the absorption within the Ag nanoparticles, both for polydisperse and monodisperse nanoparticle size distributions.

S19: Effect of MoS_2 incorporation and multiple diameter NP distribution on the Absorption of Ag for the two spacer layers Al_2O_3 and NiO_x

In addition, we have simulated the absorption characteristics of Ag NP on top of either Al_2O_3 or NiO_x on aluminum. The results show that, on both substrates, the effect of a polydisperse size distribution is a slight blue shift of the plasmon resonance compared to the resonance of a monodisperse distribution. Nonetheless, the resonance peak lies in the vicinity of the bandgap of MoS_2.

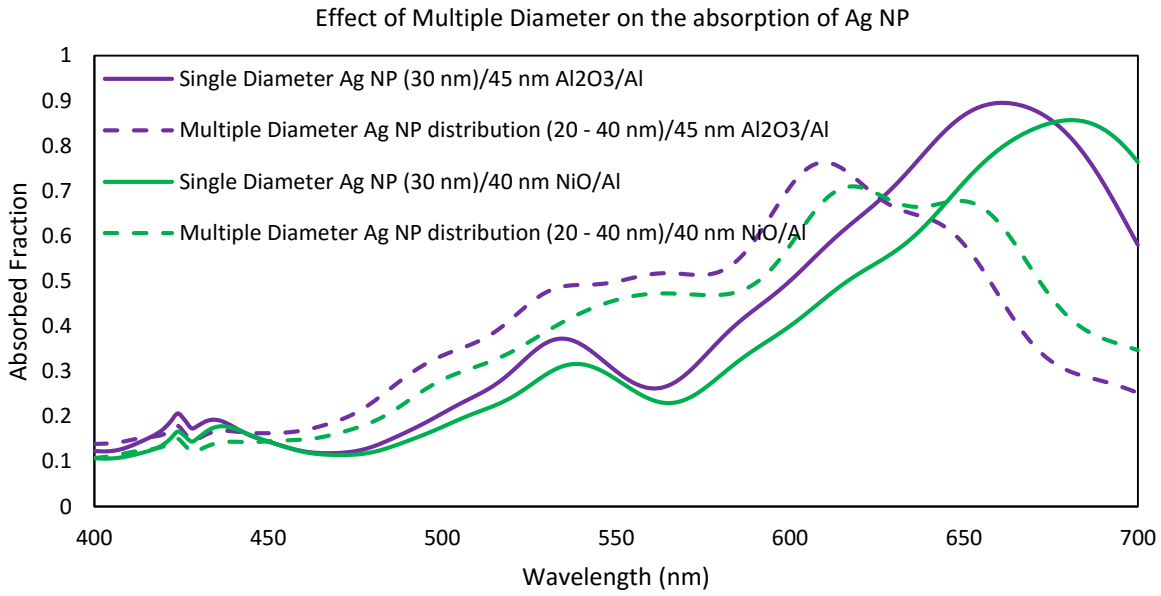

S20: Effect of a polydisperse Ag particle diameter distribution on the Absorption of MoS_2.

The experimentally measured spectrum of our plasmonic photoelectrode is broadband due to the superposition of plasmon oscillations of different sizes, shapes, densities and couplings of Ag particles. We performed additional simulations on the effect of a polydisperse Ag particle diameter distribution on the absorption of MoS_2. Specifically, we investigated whether the absorption enhancement of MoS_2 is altered significantly in the case of a polydisperse particle diameter distribution compared to a monodisperse particle diameter. To this end we simulated a unit cell which contains a polydisperse particle diameter distribution according to the histogram of particle diameters (20 nm to 40 nm) obtained from an SEM image (see below). The simulation results show that there is a negligible difference in absorption enhancement when such a unit cell is employed instead of a unit cell of single particle diameter (30 nm).

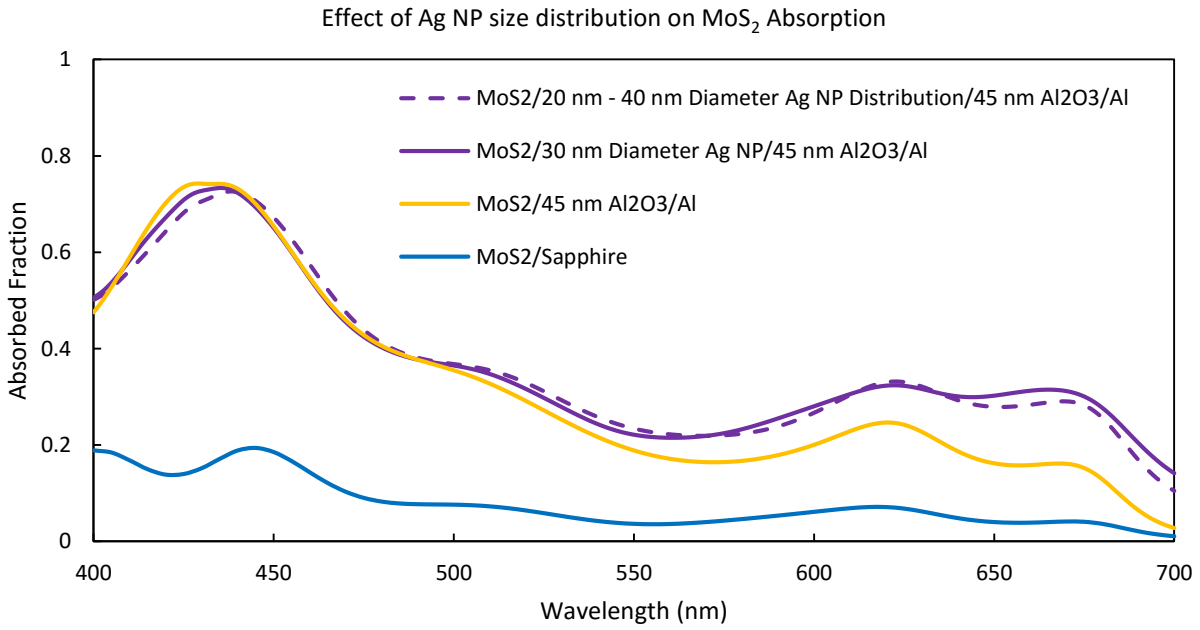

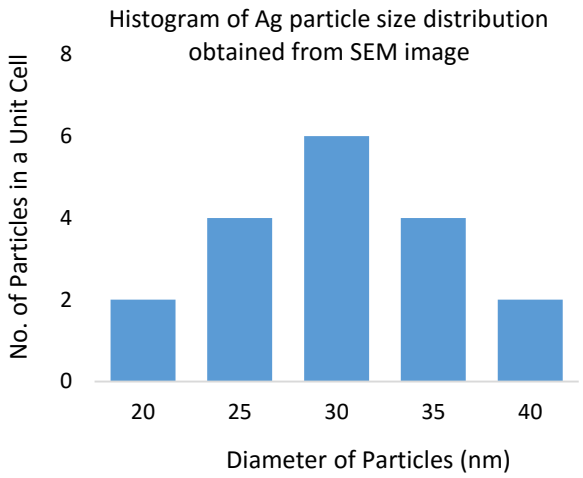

S21: Contribution of Al_2O_3/Al and NiO_x/Al substrates to the total absorption

We have determined the wavelength-dependent absorbed fraction of the Al_2O_3/ 200 nm Al and NiO_x/200 nm Al substrates by measuring the reflection (specular reflection and diffuse scattering) with an integrating sphere setup. Note, that in our structures, absorbed fraction= 1- reflected fraction, since the transmitted fraction is zero for 200 nm thick Aluminum. The results show that the contribution of the substrate to the integrated absorption (from 400 to 700 nm) is less than 19% for NiO_x/Al and around 12% for Al_2O_3/Al. NiO_x is intrinsically somewhat more absorbing due to its smaller band gap (3.5 eV, 354 nm) compared to Al_2O_3 (8.8 eV, 141 nm).

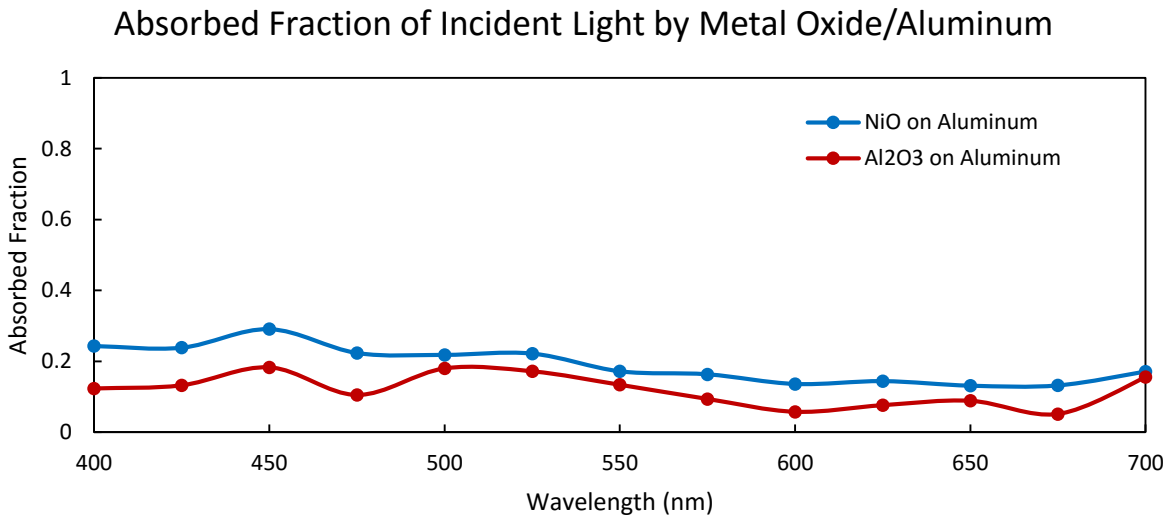

We note that NiO_x films on top of glass absorb less than 5% in the region from 400-600 nm, and approx. 0% in the region from 600 to 700 nm (see *Nano letters* 2015, 15, 6155-61, Supporting Information S5 [8]). Therefore, the majority of light absorption in NiO_x/Al and in Al_2O_3/Al occur within the Aluminum layer. This conclusion is in agreement with previous studies that have shown significant absorption near the surface-plasmon resonance of Aluminum films around 400 nm [9]. Oxide formation during e-beam evaporation of an Aluminum film is strongly dependent on the deposition rate and oxygen content/ base pressure of the ebeam evaporator vacuum chamber. It is also well known that contamination during e-beam evaporation of the Aluminum layer can lead to absorption in the visible region [10]. Studies of e-beam evaporated Aluminum films have shown that the grain size, morphology and orientation, and hence surface roughness strongly vary with the deposition rate and the base pressure/ oxygen content achieved in the e-beam evaporator vacuum chamber [11], so *the variation in scattering from different Aluminum substrates may be more influential than that from the 40 nm thick NiO_x or Al_2O_3 spacer layer*. The grain size for our ~ 200 nm Al layer is approx. 100 nm (see AFM image, Supporting Information S22). Therefore, we suggest that the scattering of our Al_2O_3/ 200 nm Al and NiO_x/200 nm Al substrates is *mainly*

determined by variations in the Aluminum roughness (instead of the roughness of our e-beam evaporated Al_2O_3 or sol-gel deposited NiO_x layer). SEM images of 40 nm NiO_x films prepared on a 200 nm Al/Si substrate are shown in the Supporting Supporting Information S3 in reference[8]. The NiO_x films are uniform and smooth, covering the grainy surface of the e-beam deposited Aluminum layer.

S22: AFM characterization of the grain size and roughness of a 200 nm thick Al film

RMS roughness ~ 3 nm. Grain size on the order of 100 nm.

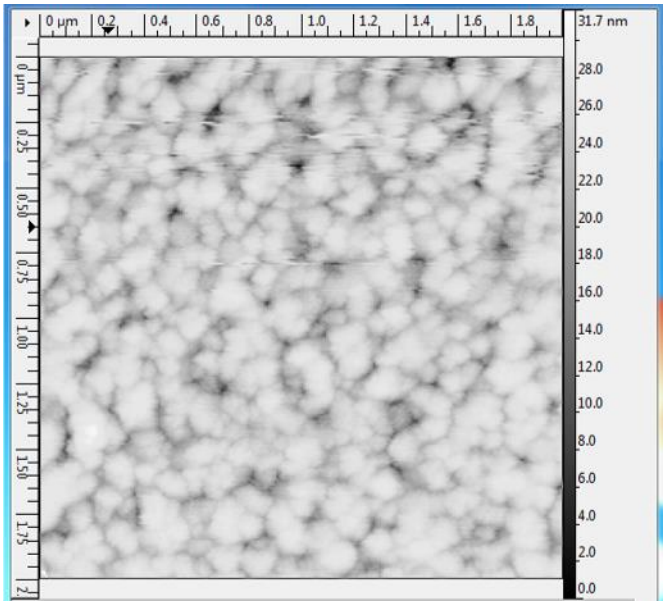

S23: Transfer process of MoS_2 on Ag NP/Spacer/Al substrate

To exfoliate the as-grown MoS_2 from SiO_2/Si sample, we drop-casted PMMA on the substrate and spun it at 3000 rpm for 40 seconds to obtain a very thin layer of PMMA on top of the MoS_2 monolayer. Then the substrate was floated in water with 3 chips of KOH. The sample was left for 12 hours and eventually the SiO_2/Si substrate sank and the PMMA+ MoS_2 layer floated up. The exfoliated MoS_2 layer was then scooped and placed on top of the Ag NP/Spacer/Al substrate. Finally, acetone, IPA and DI water were used to remove PMMA and the sample was blow-dried using N_2.

S24: Discussion of Possible Mechanisms of Photoluminescence Quenching

A shift in photoluminescence from A excitons to A- trions can be induced in MoS_2, either by altering the dielectric environment, or application of a gate bias [12,13]. This shift in photoluminescence is in both cases accompanied by (i) a reduction in photoluminescence intensity (approximately 5x in both cases) and (ii) a concomitant red-shift of the PL peak, by ~40-80 meV [13]. By contrast, in our work, a ~8 times or larger reduction in PL intensity is observed between MoS_2 on NiO_x/Al versus Al_2O_3/Al in the *absence* of any spectral shifts (<5meV within our experimental errors), inconsistent with an A→ A- shift. Furthermore, differences in dielectric screening of excitons on NiO_x/Al versus Al_2O_3/Al are highly unlikely to affect PL intensity significantly, given the miniscule difference in dielectric properties between the two materials (Al_2O_3 static dielectric constant ε= 9.34 and 11.54, NiO_x static dielectric constant ε= 11.9). By contrast, in reference [13], a change in the dielectric constant by one full unit is needed to alter the

PL intensity by only 10% for the A exciton, and the A- trion is even less sensitive. Hence, we conclude that the only plausible explanation remaining for the reduced PL intensity in the case of MoS_2/ NiO_x /Al compared to MoS_2/ Al_2O_3/Al is charge separation in the former compared to the absence of charge separation in the latter case. The energy levels of MoS_2/ NiO_x and MoS_2/ Al_2O_3 also support charge separation as an explanation for the observed photoluminescence quenching (Figure 3).

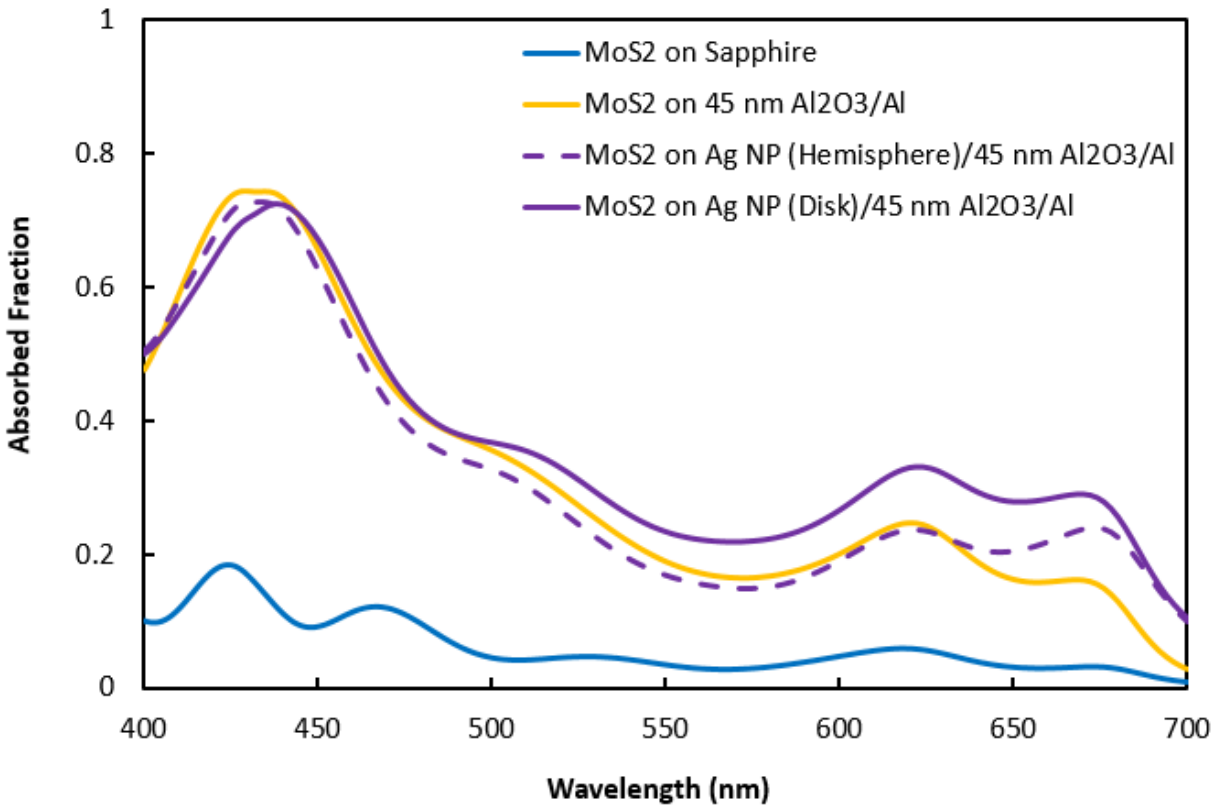

Figure S25: FDTD simulations of the particle shape dependence of the absorbed fraction as a function of wavelength.

REFERENCES

(1) Cai, W.; Shalaev, V. M.: Optical metamaterials fundamentals and applications. pp 1 online resource (xii, 200 pages).

(2) Hägglund, C.; Zeltzer, G.; Ruiz, R.; Thomann, I.; Lee, H.-B.-R.; Brongersma, M. L.; Bent, S. F. Self-Assembly Based Plasmonic Arrays Tuned by Atomic Layer Deposition for Extreme Visible Light Absorption. *Nano Lett.* **2013**, *13*, 3352-3357.

(3) Hagglund, C.; Apell, S. P. Plasmonic Near-Field Absorbers for Ultrathin Solar Cells. *J. Phys. Chem. Lett.* **2012**, *3*, 1275-1285.

(4) Liu, B.; Aydil, E. S. Growth of Oriented Single-Crystalline Rutile TiO2 Nanorods on Transparent Conducting Substrates for Dye-Sensitized Solar Cells. *J. Am. Chem. Soc.* **2009**, *131*, 3985-3990.

(5) Liu, H.; Avrutin, V.; Izyumskaya, N.; Özgür, Ü.; Morkoç, H. Transparent conducting oxides for electrode applications in light emitting and absorbing devices. *Superlattices Microstruct.* **2010**, *48*, 458-484.

(6) Tadatsugu, M. Transparent conducting oxide semiconductors for transparent electrodes. *Semicond. Sci. Technol.* **2005**, *20*, S35.

(7) He, J.; Lindström, H.; Hagfeldt, A.; Lindquist, S.-E. Dye-Sensitized Nanostructured p-Type Nickel Oxide Film as a Photocathode for a Solar Cell. *The Journal of Physical Chemistry B* **1999**, *103*, 8940-8943.

(8) Robatjazi, H.; Bahauddin, S. M.; Doiron, C.; Thomann, I. Direct Plasmon-Driven Photoelectrocatalysis. *Nano Lett.* **2015**, *15*, 6155-6161.

(9) Palik, E. D. Handbook of Optical-Constants. *J Opt Soc Am A* **1984**, *1*, p. 376.

(10) Knight, M. W.; King, N. S.; Liu, L.; Everitt, H. O.; Nordlander, P.; Halas, N. J. Aluminum for Plasmonics. *ACS Nano* **2013**.

(11) Bordo, K.; Rubahn, H. G. Effect of Deposition Rate on Structure and Surface Morphology of Thin Evaporated Al Films on Dielectrics and Semiconductors. *Mater Sci-Medzg* **2012**, *18*, 313-317.

(12) Mak, K. F.; He, K.; Lee, C.; Lee, G. H.; Hone, J.; Heinz, T. F.; Shan, J. Tightly bound trions in monolayer MoS2. *Nat. Mater.* **2013**, *12*, 207-211.

(13) Lin, Y.; Ling, X.; Yu, L.; Huang, S.; Hsu, A. L.; Lee, Y. H.; Kong, J.; Dresselhaus, M. S.; Palacios, T. Dielectric screening of excitons and trions in single-layer MoS2. *Nano Lett.* **2014**, *14*, 5569-5576.